Article

Balancing Surface Passivation and Catalysis with Integrated BiVO/(Fe-Ce)O Photoanodes in pH 9 Borate Electrolyte

Lan Zhou, Aniketa Shinde, Dan Guevarra, Francesca M. Toma, Helge Stein, John M. Gregoire, and Joel A. Haber

ACS Appl. Energy Mater., **Just Accepted Manuscript** • DOI: 10.1021/acsaem.8b01377 • Publication Date (Web): 26 Sep 2018

Balancing Surface Passivation and Catalysis with Integrated $BiVO_4$/(Fe-Ce)O_x Photoanodes in pH 9 Borate Electrolyte

Lan Zhou,[†,∥] Aniketa Shinde,[†,∥] Dan Guevarra,[†] Francesca M. Toma,[‡] Helge S. Stein,[†] John M. Gregoire,[†] Joel A. Haber[†]**

†Joint Center for Artificial Photosynthesis, California Institute of Technology, Pasadena, California 91125 (USA)

‡Chemical Sciences Division, Joint Center for Artificial Photosynthesis, Lawrence Berkeley National Laboratory; Berkeley, California 94720 (USA)

Key Words: high-throughput screening, solar fuels, oxygen evolution reaction, photoanode, bismuth vanadate.

ABSTRACT

The performance of oxygen-evolving photoanodes based on bismuth vanadate ($BiVO_4$) is critically determined by the surface coating. While these coatings passivate surface defects, transport photogenerated holes, protect against corrosion, and aid catalysis, their optimal composition changes with operating pH, thus affecting overall performance. We use high throughput photoelectrochemistry methods to map photoanode performance to enable the discovery of optimal composition and loading of Ce-rich sputter deposited $(Fe\text{-}Ce)O_x$ overlayers on undoped $BiVO_4$ in pH 9 borate buffer electrolyte. The optimal composition is found to be 20% Fe and 80% Ce with an optimal Fe + Ce metal loading of 0.9 nmol mm^{-2}. Analysis of the composition and loading dependence of (i) the photocurrent transients upon illumination toggling, (ii) stabilized photocurrent densities, and (iii) photogenerated hole transfer efficiency reveals the confluence of phenomena that give rise to the optimal performance yielding nearly perfect transfer efficiency over a narrow composition window.

TEXT

Introduction

The energy conversion efficiency of bismuth vanadate ($BiVO_4$) based photoanodes has been increased by tuning optical properties and charge mobility, transport, and separation, which have been simultaneously improved via nano and microstructuring, bulk and surface trap state mitigation, and catalyst coatings.[1-4] This continuous improvement in $BiVO_4$-based photoanodes for driving the oxygen evolution reaction (OER) owes much to the application of multifunctional

surficial catalyst coatings,[5,6] and post-synthetic treatments.[7] Although the relative importance of the mechanisms by which these coatings and treatments improve the performance of $BiVO_4$ photoanodes remains a topic of discussion,[7,8] it is clear that the coating must function as more than an OER catalyst.[6] Researchers have used multilayer coatings to achieve the benefits of catalysis, surface trap passivation, effective electrolyte interactions, and effective OER catalysis.[5,8,9] However, different solar-fuel generator device designs require OER to occur under different operating conditions including different electrolytes and pH, and discovery of optimal coatings simultaneously providing all these multiple functions under different operating conditions remains challenging. Specifically, the optimal coating composition and loading will depend upon pH and electrolyte.

For example, we previously reported high throughput experimental exploration of coating composition and loading on $BiVO_4$ photoanode performance, investigated in pH 13 electrolyte.[10-12] This pH was used for compatibility with membrane-separated, unassisted water splitting devices,[13-15] despite the inherent instability of $BiVO_4$ at this pH.[16] These investigations discovered the high performance of (Fe-Ce)O_x coatings,[11] which we further investigated using co-sputtering to produce continuous gradient composition-loading libraries on $BiVO_4$.[12] These sputter deposited films displayed even higher performance, with a maximum performance with loadings of (Fe+Ce) between 0.2 – 1.5 nmol mm^{-2} and 20-30% Fe content in 0.1 M NaOH electrolyte. Unfortunately, the coating provided limited corrosion protection, with significant loss in performance within an hour of photoelectrochemical operation. Recently, solar fuels generators utilizing bipolar membranes have mitigated the requirement for strongly acidic or basic pH at the photoanode in membrane-separated devices.[17-20] In particular, a highly efficient generator was reported wherein the photoanode was operated in pH 9 borate buffer electrolyte.[17]

Therefore, exploration of the trends in photoelectrochemical performance of composite photoanodes in multiple electrolytes is of fundamental importance, as the stability and interface chemistry of both the light absorbing semiconductor and OER catalyst will vary with pH and electrolyte composition, as well as the detailed mechanism for the 4 electron, 4 proton OER.[8,21]

Herein, we investigate an (Fe-Ce)O_x composition-loading coating library on undoped $BiVO_4$ in a pH 9 borate electrolyte and compare the performance of this library to one previously studied in pH 13 sodium hydroxide electrolyte. Interestingly, $BiVO_4$ is reported to have enhanced stability in borate buffer at pH 9,[22-24] and the discovery of novel, optimal coating compositions in this electrolyte may open new applications of this material in photoelectrochemical devices for artificial photosynthesis. Our analysis demonstrates that this coating composition yields similar performance at pH 9 to that observed at pH 13 largely due to the role of Ce in passivating $BiVO_4$ surface defects; however, the optimal performance shifts to a narrower range of coating compositions at pH 9 relative to pH 13. Comparison of how the coating composition and loading impact charge transfer efficiency via analysis of current transients in the toggled illumination J-E curves at both pH 9 and pH 13 provides insight into the causes for the reduced range of composition and loading producing high performance in pH 9.

Results and Discussion

The preparation of the (Fe-Ce)O_x coating library on the undoped $BiVO_4$ substrate was performed as reported previously for the library analyzed using 0.1 M NaOH electrolyte.[12] The 10 cm × 10 cm $BiVO_4$ film on fluorine doped tin oxide (FTO) coated glass was prepared by multiple spin coatings of precursors with intermediate thermal oxidation, as previously described.[10] X-ray diffraction (XRD) was used to confirm phase-pure monoclinic $BiVO_4$. The

(Fe-Ce)O_x coating was deposited as a continuous composition and loading gradient library using a non-confocal geometry for the 2-target (Fe and Ce) radio-frequency (RF) magnetron co-sputtering in a reactive atmosphere composed of 0.64 Pa Ar and 0.16 Pa O_2, with no intentional heating during deposition, as described previously.[12,25] The photoelectrochemical performance was measured in borate buffer (pH 9, 0.1 M boric acid with 0.05 M potassium hydroxide) using the previously described scanning drop electrochemical cell (SDC),[26] with a 0.02 V s^{-1} CV and 0.5 Hz toggled illumination (1.34 s on, 0.67 s off) utilizing a fiber optic-coupled xenon lamp illuminating 1 mm diameter sample spots.[10] In total, 339 samples were measured spaced 5 mm apart on a square grid over the 10 cm × 10 cm (Fe-Ce)O_x / $BiVO_4$ area. The electrochemical power generation P_{max} (or power saved[27] compared to an ideal electrocatalyst operating at the Nernstian potential) was calculated as the product of the reverse bias potential and the corresponding photocurrent.

The scanning drop electrochemical cell used to acquire the toggled illumination photoelectrochemical data is depicted schematically in Figure 1a. Typical data for the anodic sweep of the toggled illumination CVs are displayed in Figure 1b, from which the J-E curves displayed in Figure 1c are extracted. The series of coatings for which this data was acquired all have a metal loading of approximately 0.9 nmol mm^{-2} and span most of the library's composition range. Current transients are apparent when light is toggled on at all compositions, as well as toggled off for compositions containing ≥ 21% Fe. Some of these transient spikes appear to be too brief to be sufficiently captured by the 20 Hz data acquisition frequency, while relatively long-duration transients are observed at high Fe concentration. Our data analysis for extracting the quasi-steady state photocurrent only utilizes the average photocurrent over the final 0.74 seconds of the illuminated pulse, where the contributions from transients are negligible. The

stabilized average photocurrents for each illumination cycle are shown as solid circles in Figure 1c, which are fit using an empirical model to generate the fitted quasi-steady state J-E curve for each library sample, as described previously and in the SI.[10] Each J-E curve is further analyzed to extract the figures of merit (FOM) displayed in Figure 2.

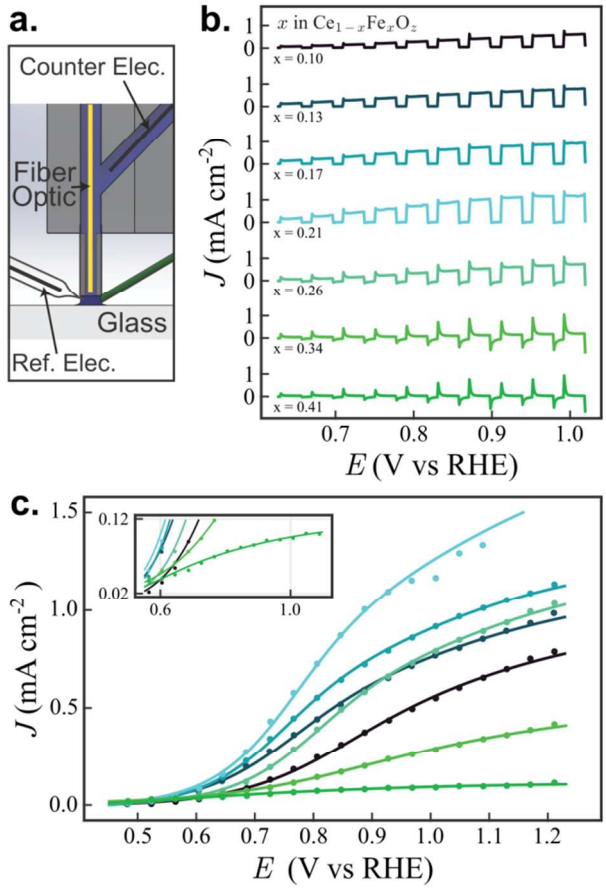

Figure 1. (a) Schematic drawing of the fiber optic-coupled scanning drop electrochemical cell. (b) Representative anodic sweep toggled-illumination CV data collected at near-constant total metal loading of 0.9 nmol mm^{-2}, including the coating with optimal composition and loading. The data traces refer to different concentrations of Fe in $Ce_{1-x}Fe_xO_z$, and are color-coordinated with the circles indicating the sample positions in composition-loading space in Figure 2a. (c) The photo-J-E curves extracted from the data in panel (b) using automated fitting algorithms (for

details see Table S1 in SI).[10] The inset expands the low E region of the curves to focus on the curve inflection points.

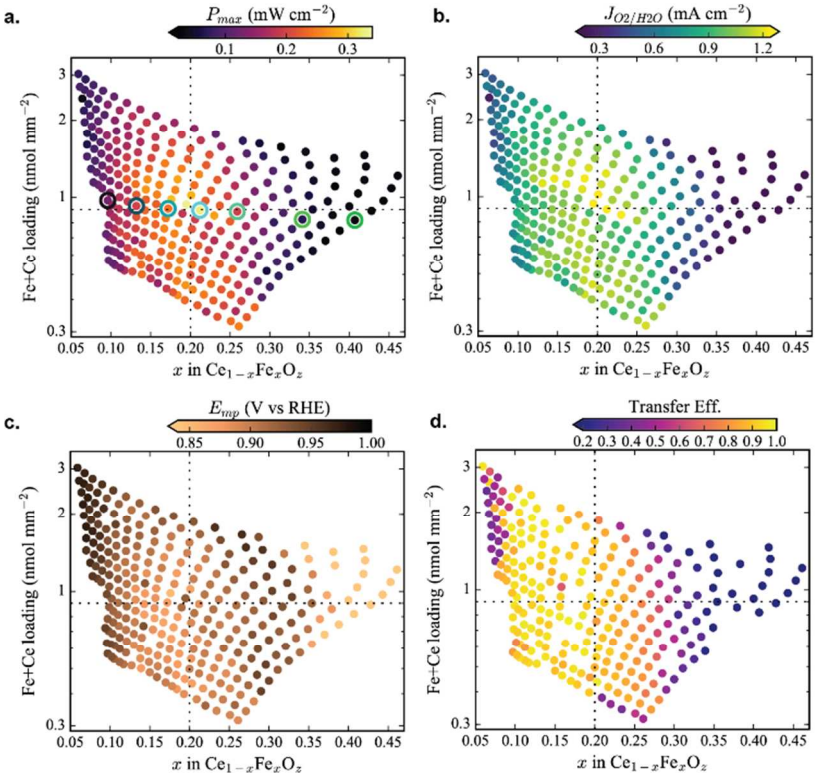

Figure 2. Extracted FOMs mapped in the coating composition and loading space. (a) P_{max}, the maximum photoelectrochemical power generated, (b) $J_{O2/H2O}$, the photocurrent density generated at the Nernstian OER potential (1.23 V vs RHE), (c) E_{mp}, the potential of the maximum power point for each sample, as extracted from the fitted J-E curves as represented in Figure 1c. Panel (d) displays the transfer efficiency of photo-generated holes to the electrolyte extracted from the ratio of peak transient photocurrent to stabilized photocurrent at the E_{mp} of each sample (see the SI for procedures).

We use P_{max} as the primary FOM for photoanode performance, because it incorporates the three other primary quality factors for the photoelectrode. That is, P_{max} combines the photovoltage, photocurrent, and fill factor into a single scalar quantity that is pertinent to device performance. The highest P_{max} is produced at a metal loading (Fe + Ce) of 0.9 nmol mm^{-2} and a composition of 20 mol% Fe (indicated by the dashed horizontal lines and dashed vertical lines in each panel of Figure 2). Values of P_{max} within about 30% of the maximum value can be obtained over the 15-25 mol% Fe composition window for all loadings below about 1.4 nmol mm^{-2}. A sample in the middle of this composition-loading space (20% Fe concentration and 0.5 nmol mm^{-2} loading) was chosen for stability characterization via a toggled illumination CA measurement at 1.23 V vs RHE for 30 minutes, yielding a ~40% decrease in photocurrent (shown in Figure S1), likely due to a non-conformal coating that permits electrolyte contact to the $BiVO_4$ and thus gradual corrosion of the absorption layer.

A deeper understanding of how the surface coating alters and improves the photoanode performance is gained from inspection of the E_{mp} and $J_{O2/H2O}$ trends in Figure 2. Relative to the coating with highest P_{max}, more Ce-rich compositions have a reduced P_{max} primarily due to a reduction in $J_{O2/H2O}$, but also due to a lower apparent photovoltage, yielding an E_{mp} closer to the OER Nernstian potential. $J_{O2/H2O}$ varies more considerably over the coating library (0.2-1.3 mA cm^{-2}) compared to E_{mp} and is thus the dominant factor in determining P_{max}.

To further explore the origins of these trends, we return to inspection of individual J-E curves in Figure 1c. The toggled illumination J-E data from which these J-E curves were extracted are presented in Figure 1b. The color-matched circles in Figure 2a indicate the coating composition and loading for each of the specific measurements (near optimal metal loading and across the full range of compositions) shown in Figure 1b and c. As is apparent in Figure 1c, the J-E curve from

the optimal coating composition and loading has the greatest photocurrent density at all potentials, but coating compositions which are more Ce-rich actually exhibit superior fill factors, despite lower photocurrent densities. In contrast, more Fe-rich coating compositions produced both poor fill factors and much lower photocurrent densities. Figure 2d represents the photo-carrier transfer efficiency for water oxidation at pH 9 as a ratio of the fitted exponential value of the current transient at illumination-on to the stabilized photocurrent for the illumination cycle at the E_{mp} for each sample. Notably, for coating compositions with the highest fill factors, slightly Ce-rich relative to the compositions with the highest P_{max} performance, the transfer efficiency approaches 1.0 and the algorithm fails because there is no current transient to fit, as indicated by the absent data points in Figure 2d. On the other hand, for coating compositions with the highest P_{max} (20% Fe) there are noticeable photocurrent transients in Figure 1b and a transfer efficiency of ~0.9 in Figure 2d. These trends indicate a balance between surface passivation and effective OER catalysis over this range of coating compositions.

As can be seen in Figure 1b, the transient signals upon toggling illumination, which are indicative of populating and depopulating surface trap states,[28] also increase with increasing mole fraction of Fe in the coating beyond the optimal composition. The coatings with the lowest Fe content (10 mol%) display very short transients which quickly decay to the sustained photocurrent density values. This finding indicates that the Ce-rich oxides provide some passivation of $BiVO_4$ surface states, which has been demonstrated to be the primary role of catalyst coatings on $BiVO_4$.[6] However, an optimal coating must also catalyze the OER at the effective hole potential provided by $BiVO_4$. Apparently, the Ce-rich coating is a sufficiently poor catalyst that the photocurrent is suppressed by the slow OER. At the highest performing coating composition (light blue in Figure 1) small transients are apparent upon illumination, but the 20

mol% Fe provides sufficient catalytic activity to elevate the photocurrent density to twice that of the most Ce-rich compositions. At higher Fe compositions, the transients are more pronounced, resulting in decay to near zero photocurrent within 0.2 s of photoanode illumination. While the higher Fe concentration may dilute the Ce passivation of the $BiVO_4$ surface states, we also note that charging of trap states within a coating has been discussed as a contributor to photocurrent transients, with thicker coatings resulting in longer time constants.[29] Thus, the large photocurrent transients observed for the coatings containing larger concentrations of Fe may indicate bulk oxidation (light on) and reduction (light off) of the coating itself. This trend is contrary to the report of excellent surface passivation with electrodeposited FeOOH,[5] which may be due to the presence of Fe^{+2} and its reversible oxidation to Fe^{+3} in the sputter deposited coatings, motivating development of surface coating techniques that combine CeO_2 with FeOOH.

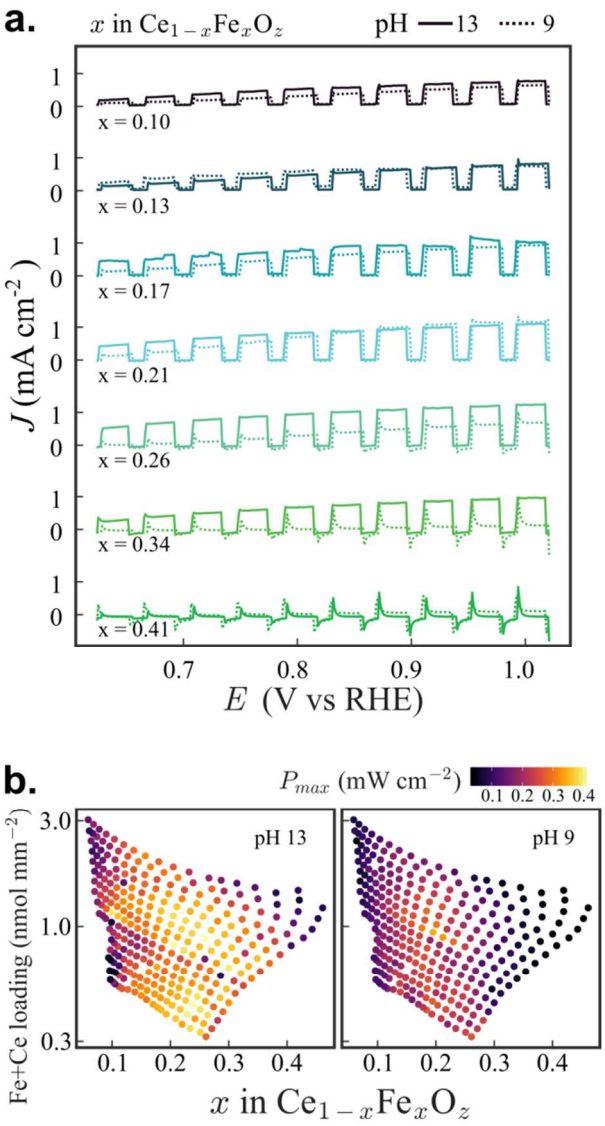

Figure 3. (a) Overlay of anodic sweep toggled-illumination CV data collected using pH 9 (displayed in Figure 1b) and pH 13 electrolyte at similar loading and compositions with increasing Fe concentration in the $Ce_{1-x}Fe_xO_z$ coating on $BiVO_4$. The current transients are far more pronounced in pH 9 than in pH 13 at all but the most Fe-rich composition (34% Fe). (b) Extracted P_{max} mapped in the coating composition and loading space for duplicate coating libraries characterized in pH 13 and pH 9.

By overlaying the toggled-illumination CV curves for duplicate photoanode assemblies evaluated in pH 9 and pH 13 electrolytes, a distinct difference in coating performance as a function of composition becomes apparent. Specifically, the pronounced photocurrent transients previously noted for most coating compositions in pH 9 electrolyte are mostly absent in the pH 13 electrolyte. In pH 13 electrolyte, the CVs from x = 0.17 to x = 0.34 reveal that similar performance is obtained over this 17 at.% range, while only 2 CVs in pH 9 exhibit similar performance (x = 0.17 and 0.21), demonstrating the need for much more precise optimization in pH 9 electrolyte. The passivation of surface trap states is particularly sensitive to composition in pH 9, indicating that the surface/interface chemistry changes either the surface passivation or the mechanism/rate of the OER, relative to pH 13 electrolyte.

Figure 3b further illustrates the pH-dependent relationships between PEC performance and the coating composition and loading, with the P_{max}, for pH 13 and pH 9 on a common color scale. In pH 13 electrolyte, the P_{max} is high over a large range of coating composition and loading, consistent with the small photocurrent transients indicative of low recombination via trap states. In contrast, although the highest P_{max} obtained in pH 9 approaches that obtained in pH 13, the highest P_{max} values are produced over a narrower range of coating compositions and loadings having relatively small photocurrent transients and high, stabilized photocurrent densities. A slight shift in the optimal composition and loading from 26% Fe and 1 nmol mm^{-2} loading at pH 13 to the more Ce-rich 20% Fe and 0.9 nmol mm^{-2} loading at pH 9 is observed, but values of P_{max} in each electrolyte span a similar range. At pH 13, P_{max} ranges from approximately 0.04 to 0.38 mW cm^{-2} over the coating library, while at pH 9 P_{max} ranges from approximately 0.05 to 0.33 mW cm^{-2}.

Comparison FOM plots for $J_{O2/H2O}$, fill factor, and E_{mp} at pH 13 and pH 9 are shown in Figure S2 in the SI. The surface trap recombination processes which produce the sharp current transients observed in Figure 3, lead to reduced stabilized photocurrents, which is also reflected in the $J_{O2/H2O}$ FOM plots in Figure S2a. As noted above, the magnitude of $J_{O2/H2O}$ varies over the largest range of values and is the primary contributor to variation in the P_{max} plotted in Figure 3b. The fill factor also has a more focused region of high values at pH 9 than at pH 13 (Figure S2b), likely arising from the increased recombination at surface trap states with lower applied potential aiding the extraction of the photogenerated holes. The E_{mp} at pH 9 is generally lower than at pH 13, but the variation with composition and loading is less pronounced than observed for $J_{O2/H2O,}$ Figure S2c. The overpotential required to drive the OER increases with decreasing pH, therefore the E_{mp} (and consequently the power conversion efficiency) may decrease at pH 9 relative to pH 13. Given the deep valance band of $BiVO_4$,[6] the loss in P_{max} due to increased OER overpotential can be mitigated if the catalyst coating provides efficient hole transport, and the present work demonstrates that while coating performance varies with pH, certain optimized coatings can retain excellent PEC performance in pH 9 electrolyte.

The shifting of optimal coating performance to a narrower composition space in pH 9 electrolyte relative to pH 13 may relate to differences in surface or interface chemistry or in OER mechanisms at the 2 pH values. The surface chemistry of metal oxides is fundamentally dependent upon pH. Recent literature has reported that for $BiVO_4$(010) the point of zero charge is at pH 3.46, consistent with experimental values of 2.5-3.5.[30] Further, calculation of the surface coverage of water molecules or of OH^- indicates that pH 9 is in a transition zone between the OH^- and H_2O water oxidation mechanisms, while pH 13 is clearly in the OH^- regime.[31] However, the experimental points of zero charge for the coating oxides is significantly higher, in

the range of pH 5-8 for CeO_2 and pH 7-9 for various iron oxides.[32] Thus, a significant difference in surface speciation of the metal oxide coating may be present at pH 9 relative to pH 13, thereby altering the operative OER reaction mechanism at these pH values. Further, the rate of the OER decreases simply because the concentration of the OH^-(aq) reactant is decreased by 4 orders of magnitude at pH 9 relative to pH 13, requiring a more precise coating composition to balance the passivation of surface traps and OER catalysis.

Conclusions

The performance of photoanodes as a function of composition and loading of a continuous gradient (Fe-Ce)O_x coating on undoped $BiVO_4$ is evaluated in pH 9 borate buffer and compared to nominally-identical photoanode assemblies evaluated in pH 13 sodium hydroxide electrolyte. In both electrolytes the performance of the photoanode assembly varies by an order of magnitude over the composition range 10 to 40 mol% Fe with relatively little sensitivity to the total loading of the metal coating from 0.3 to 3 nmol mm^{-2}. The characterization of both transient and stabilized photocurrent with coating composition reveal the importance of Ce for $BiVO_4$ surface passivation and Fe for OER catalysis, with the $Ce_{0.8}Fe_{0.2}O_x$ composition providing the optimal balance of these phenomena and thus optimal photoelectrochemical power generation. The PEC performance is much more sensitive to composition in pH 9 electrolyte than pH 13, with the optimal window of only ~5at.%, highlighting the need for combinatorial methods to identify optimal interfaces between light absorbers and catalysts in each selected electrolyte.

ASSOCIATED CONTENT

Supporting Information. Supporting Information is available free of charge: Experimental Details, Stability characterization, Comparison of $J_{O2/H2O}$, fill factor, and E_{mp} at pH 13 and pH 9

as a function of coating composition and loading, Table of numerical values of plotted figures of merit (FOMs) at pH 9.

AUTHOR INFORMATION

Corresponding Authors

*E-mail: gregoire@caltech.edu; jahaber@caltech.edu.

Author Contributions

The manuscript was written through contributions of all authors. All authors have given approval to the final version of the manuscript. ‖L.Z. and A. S. contributed equally to this work.

Funding Sources

This material is based upon work performed by the Joint Center for Artificial Photosynthesis, a DOE Energy Innovation Hub, supported through the Office of Science of the U.S. Department of Energy under Award Number DE-SC0004993.

REFERENCES

(1) Huang, Z. F.; Pan, L.; Zou, J. J.; Zhang, X. W.; Wang, L. Nanostructured Bismuth Banadate-Based Materials for Solar-Energy-Driven Water Oxidation: A Review on Recent Progress. *Nanoscale* **2014**, *6*, 14044-14063.

(2) Tan, H. L.; Amal, R.; Ng, Y. H. Alternative Strategies in Improving the Photocatalytic and Photoelectrochemical Activities of Visible Light-Driven $BiVO_4$: A Review. *J. Mater. Chem. A* **2017**, *5*, 16498-16521.

(3) Tolod, K. R.; Hernandez, S.; Russo, N. Recent Advances in the $BiVO_4$ Photocatalyst for Sun-Driven Water Oxidation: Top-Performing Photoanodes and Scale-Up Challenges. *Catalysts* **2017**, *7*.

(4) Park, Y.; McDonald, K. J.; Choi, K. S. Progress in Bismuth Vanadate Photoanodes for use in Solar Water Oxidation. *Chem. Soc. Rev.* **2013**, *42*, 2321-2337.

(5) Kim, T. W.; Choi, K. S. Nanoporous $BiVO_4$ Photoanodes with Dual-Layer Oxygen Evolution Catalysts for Solar Water Splitting. *Science* **2014**, *343*, 990-994.

(6) Zachaus, C.; Abdi, F. F.; Peter, L. M.; van de Krol, R. Photocurrent of $BiVO_4$ is Limited by Surface Recombination, not Surface Catalysis. *Chem. Sci.* **2017**, *8*, 3712-3719.

(7) Lamm, B.; Trzesniewski, B. J.; Doscher, H.; Smith, W. A.; Stefik, M. Emerging Postsynthetic Improvements of $BiVO_4$ Photoanodes for Solar Water Splitting. *Acs Energy Lett.* **2018**, *3*, 112-124.

(8) Ding, C. M.; Shi, J. Y.; Wang, Z. L.; Li, C. Photoelectrocatalytic Water Splitting: Significance of Cocatalysts, Electrolyte, and Interfaces. *Acs Catal.* **2017**, *7*, 675-688.

(9) Hu, Y. F.; Wu, Y. Q.; Feng, J. Y.; Huang, H. T.; Zhang, C. C.; Qian, Q. F.; Fang, T.; Xu, J.; Wang, P.; Li, Z. S.; Zou, Z. G. Rational Design of Electrocatalysts for Simultaneously Promoting Bulk Charge Separation and Surface Charge Transfer in Solar Water Splitting Photoelectrodes. *J. Mater. Chem. A* **2018**, *6*, 2568-2576.

(10) Guevarra, D.; Shinde, A.; Suram, S. K.; Sharp, I. D.; Toma, F. M.; Haber, J. A.; Gregoire, J. M. Development of Solar Fuels Photoanodes Through Combinatorial Integration of Ni-La-Co-Ce Oxide Catalysts on $BiVO_4$. *Energy Environ. Sci.* **2016**, *9*, 565-580.

(11) Shinde, A.; Guevarra, D.; Liu, G. J.; Sharp, I. D.; Toma, F. M.; Gregoire, J. M.; Haber, J. A. Discovery of Fe-Ce Oxide/$BiVO_4$ Photoanodes through Combinatorial Exploration of Ni-Fe-Co-Ce Oxide Coatings. *Acs Appl. Mater. Interfaces* **2016**, *8*, 23696-23705.

(12) Shinde, A.; Li, G.; Zhou, L.; Guevarra, D.; Suram, S. K.; Toma, F. M.; Yan, Q.; Haber, J. A.; Neaton, J. B.; Gregoire, J. M. The Role of the CeO_2/$BiVO_4$ Interface in Optimized Fe-Ce Oxide Coatings for Solar Fuels Photoanodes. *J. Mater. Chem. A* **2016**, *4*, 14356-14363.

(13) Singh, M. R.; Papadantonakis, K.; Xiang, C. X.; Lewis, N. S. An Electrochemical Engineering Assessment of the Operational Conditions and Constraints for Solar-Driven Water-Splitting Systems at Near-Neutral pH. *Energy Environ. Sci.* **2015**, *8*, 2760-2767.

(14) Verlage, E.; Hu, S.; Liu, R.; Jones, R. J. R.; Sun, K.; Xiang, C. X.; Lewis, N. S.; Atwater, H. A. A Monolithically Integrated, Intrinsically Safe, 10% Efficient, Solar-Driven Water-Splitting System Based on Active, Stable Earth-Abundant Electrocatalysts in Conjunction with Tandem III-V Light Absorbers Protected by Amorphous TiO_2 Films. *Energy Environ. Sci.* **2015**, *8*, 3166-3172.

(15) Xiang, C. X.; Weber, A. Z.; Ardo, S.; Berger, A.; Chen, Y. K.; Coridan, R.; Fountaine, K. T.; Haussener, S.; Hu, S.; Liu, R.; Lewis, N. S.; Modestino, M. A.; Shaner, M. M.; Singh, M. R.; Stevens, J. C.; Sun, K.; Walczak, K. Modeling, Simulation, and Implementation of Solar-Driven Water-Splitting Devices. *Angew. Chem., Int. Ed.* **2016**, *55*, 12974-12988.

(16) Toma, F. M.; Cooper, J. K.; Kunzelmann, V.; McDowell, M. T.; Yu, J.; Larson, D. M.; Borys, N. J.; Abelyan, C.; Beeman, J. W.; Yu, K. M.; Yang, J. H.; Chen, L.; Shaner, M. R.; Spurgeon, J.; Houle, F. A.; Persson, K. A.; Sharp, I. D. Mechanistic Insights into Chemical and Photochemical Transformations of Bismuth Vanadate Photoanodes. *Nat. Com.* **2016**, *7*.

(17) Sun, K.; Liu, R.; Chen, Y. K.; Verlage, E.; Lewis, N. S.; Xiang, C. X. A Stabilized, Intrinsically Safe, 10% Efficient, Solar-Driven Water-Splitting Cell Incorporating Earth-Abundant Electrocatalysts with Steady-State pH Gradients and Product Separation Enabled by a Bipolar Membrane. *Adv. Energy Mater.* **2016**, *6*.

(18) Luo, J. S.; Vermaas, D. A.; Bi, D. Q.; Hagfeldt, A.; Smith, W. A.; Gratzel, M. Bipolar Membrane-Assisted Solar Water Splitting in Optimal pH. *Adv. Energy Mater.* **2016**, *6*.

(19) Schreier, M.; Heroguel, F.; Steier, L.; Ahmad, S.; Luterbacher, J. S.; Mayer, M. T.; Luo, J. S.; Gratzel, M. Solar Conversion of CO_2 to CO using Earth-Abundant Electrocatalysts Prepared by Atomic Layer Modification of CuO. *Nat. Energy* **2017**, *2*.

(20) Zhou, X. H.; Liu, R.; Sun, K.; Chen, Y. K.; Verlage, E.; Francis, S. A.; Lewis, N. S.; Xiang, C. X. Solar-Driven Reduction of 1 atm of CO_2 to Formate at 10% Energy-Conversion

Efficiency by Use of a TiO_2-Protected III-V Tandem Photoanode in Conjunction with a Bipolar Membrane and a Pd/C Cathode. *Acs Energy Lett.* **2016**, *1*, 764-770.

(21) Reier, T.; Nong, H. N.; Teschner, D.; Schlögl, R.; Strasser, P. Electrocatalytic Oxygen Evolution Reaction in Acidic Environments – Reaction Mechanisms and Catalysts. *Adv. Energy Mater.* **2017**, *7*, 1601275.

(22) Lee, D. K.; Choi, K. S. Enhancing Long-Term Photostability of $BiVO_4$ Photoanodes for Solar Water Splitting by Tuning Electrolyte Composition. *Nat. Energy* **2018**, *3*, 53-60.

(23) Kuang, Y. B.; Jia, Q. X.; Nishiyama, H.; Yamada, T.; Kudo, A.; Domen, K. A Front-Illuminated Nanostructured Transparent $BiVO_4$ Photoanode for > 2% Efficient Water Splitting. *Adv. Energy Mater.* **2016**, *6*.

(24) Lamm, B.; Sarkar, A.; Stefik, M. Surface functionalized atomic layer deposition of bismuth vanadate for single-phase scheelite. *J. Mater. Chem. A* **2017**, *5*, 6060-6069.

(25) Suram, S. K.; Zhou, L.; Becerra-Stasiewicz, N.; Kan, K.; Jones, R. J. R.; Kendrick, B. M.; Gregoire, J. M. Combinatorial Thin Tilm Composition Mapping Using Three Dimensional Deposition Profiles. *Rev. Sci. Instrum.* **2015**, *86*.

(26) Gregoire, J. M.; Xiang, C. X.; Liu, X. N.; Marcin, M.; Jin, J. Scanning Droplet Cell for High Throughput Electrochemical and Photoelectrochemical Measurements. *Rev. Sci. Instrum.* **2013**, *84*.

(27) Coridan, R. H.; Nielander, A. C.; Francis, S. A.; McDowell, M. T.; Dix, V.; Chatman, S. M.; Lewis, N. S. Methods for Comparing the Performance of Energy-Conversion Systems for use in Solar Fuels and Solar Electricity Generation. *Energy Environ. Sci.* **2015**, *8*, 2886-2901.

(28) Zhong, D. K.; Choi, S.; Gamelin, D. R. Near-Complete Suppression of Surface Recombination in Solar Photoelectrolysis by "Co-Pi" Catalyst-Modified W:$BiVO_4$. *J. Am. Chem. Soc.* **2011**, *133*, 18370-18377.

(29) Klahr, B.; Gimenez, S.; Fabregat-Santiago, F.; Bisquert, J.; Hamann, T. W. Photoelectrochemical and Impedance Spectroscopic Investigation of Water Oxidation with "Co-Pi"-Coated Hematite Electrodes. *J. Am. Chem. Soc.* **2012**, *134*, 16693-16700.

(30) Ambrosio, F.; Wiktor, J.; Pasquarelloe, A. pH-Dependent Surface Chemistry from First Principles: Application to the $BiVO_4$(010)-Water Interface. *Acs Appl. Mater. Interfaces* **2018**, *10*, 10011-10021.

(31) Ambrosio, F.; Wiktor, J.; Pasquarello, A. pH-Dependent Catalytic Reaction Pathway for Water Splitting at the $BiVO_4$-Water Interface from the Band Alignment. *Acs Energy Lett.* **2018**, *3*, 829-834.

(32) Kosmulski, M. The pH Dependent Surface Charging and Points of Zero Charge. VII. Update. *Adv. Colloid Interface Sci.* **2018**, *251*, 115-138.

Table of Contents Graphic